JACS
JOURNAL OF THE AMERICAN CHEMICAL SOCIETY

Communication

pubs.acs.org/JACS

# A Dark-Field Scattering Spectroelectrochemical Technique for Tracking the Electrodeposition of Single Silver Nanoparticles

Caleb M. Hill and Shanlin Pan*

Department of Chemistry, The University of Alabama, Tuscaloosa, Alabama 35487, United States

Supporting Information

**ABSTRACT:** Dark-field scattering spectroelectrochemistry is used to analyze the electrochemical formation of individual Ag nanoparticles (NPs) at the surface of an indium tin oxide electrode. Heterogeneities in redox potentials among NPs not visible in bulk electrochemical measurements are presented for the first time. Through correlated electron microscopy, single NP light scattering intensity is related to particle size according to Mie theory, enabling rapid particle size determination and the construction of voltammetric curves for individual NPs.

For any quantitative analytical technique, a single analyte or single chemical reaction event represents the ultimate attainable limit of detection. This may come in the form of an atom, a molecule, a nanoparticle (NP), a defect site on a crystal surface, or a single molecule undergoing a redox reaction at a bulk electrode. There are inherent advantages to measurements at this limit, a primary one being the ability to thoroughly characterize heterogeneities in structure or reactivity that would only manifest in ensemble measurements as the broadening of peaks. In the electrodeposition of NPs, for example, traditional electrochemical measurements can be used to calculate the total quantity of material deposited through Faraday's law. If the number and shape of particles are known, an average size can be obtained easily. However, information on the resulting size distribution cannot be directly obtained through such measurements. We present in this report a spectroelectrochemical method employing dark-field scattering (DFS) microscopy capable of tracking the deposition of individual Ag NPs and NP clusters *in situ* with high spatial (~350 nm) and temporal (millisecond) resolution. This method can be used to track the deposition of several hundreds to thousands of NPs simultaneously and reconstruct their voltammetric curves at the single NP level, feats not possible through existing electrochemical techniques.

Methods capable of resolving electrochemical reactions occurring at individual nanostructures are critical to accurately determining their structure–function relationships. The direct electrochemical detection of single NPs has been demonstrated via a current amplification scheme as they collide at a microelectrode.[1] More recently, heterogeneities in the catalytic activity of single metal NPs[2−4] and the charge-transfer performance of individual conjugated polymer molecules/NPs[5−7] have been studied using fluorescence-based single molecule spectroelectrochemical (SMS-EC) methods. Tao et al. have developed a surface plasmon resonance (SPR)-based imaging technique

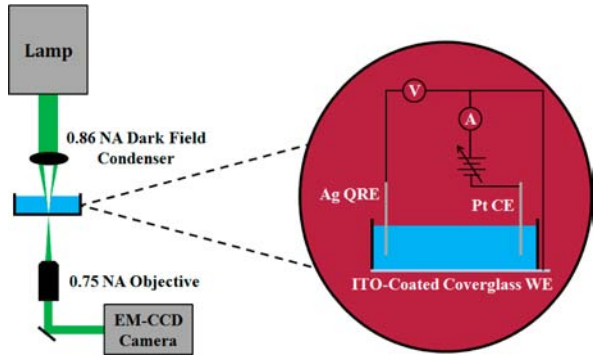


**Figure 1.** Experimental setup for the dark-field scattering spectroelectrochemistry experiments.

capable of measuring local electrochemical currents down to the single NP level by exploiting the sensitivity of SPR to the local dielectric environment.[8−10] The DFS method presented here is similar to the SPR method of Tao et al. in that the measured signal is attributable to the interaction of light with plasmons, but the change in signal in the DFS method is dominated by the modification of the metal nanostructure geometry rather than changes in dielectric environment. Neither the reported SPR imaging techniques nor the other aforementioned SMS-EC methods have been employed to directly observe the synthesis of individual NPs.

The DFS spectroscopy of individual metallic nanostructures (primarily Ag and Au) has been heavily studied and reported in the literature.[11−22] This is due to the technique's ability to directly probe the plasmonic properties of individual structures; correlation with electron microscopy is usually carried out, which allows for the rigorous testing of theoretical structure–function relationships. The most commonly reported studies concentrate on the spectral profiles of individual nanostructures. Recently, Link et al. reported the correlation of scattering intensity of individual nanostructures with their size, which agreed well with the well-known Mie solution for the scattering of electromagnetic radiation by metallic particles.[23] This is the strategy we employ in the analysis presented here, as the correlation of intensity with particle geometry allows for single particle measurements to be carried out easily in a wide-field configuration.

The experimental setup can be seen in Figure 1. Ag particles were deposited from MeCN containing Ag acetate and $LiClO_4$ by

**Received:** July 25, 2013
**Published:** October 31, 2013

   dx.doi.org/10.1021/ja4075387 | *J. Am. Chem. Soc.* 2013, 135, 17250−17253

ramping the indium tin oxide (ITO) electrode potential cathodically (~0.1 to −0.2 V vs SHE). Simultaneously, light scattering at the electrode surface was imaged over a ~100 $\mu$m × 100 $\mu$m sample area. Upon the application of sufficiently cathodic potentials, light scattering due to the presence of deposited Ag NPs on the ITO electrode becomes detectable. This can be seen visually in the inset images in Figure 2, given at the indicated

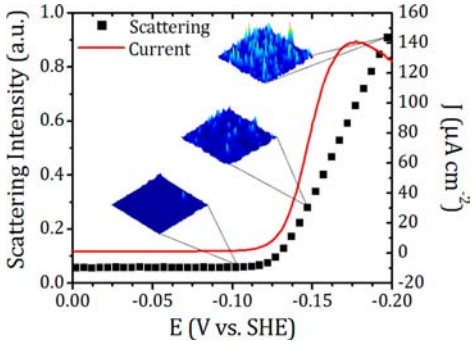


**Figure 2.** Total measured scattering intensity and bulk current density during the potential sweep. The insets are scattering images (~40 $\mu$m × 40 $\mu$m) at the indicated points along the sweep.

points along the sweep. The total measured scattering intensity and measured electrode current are included for reference. This total scattering intensity across the electrode surface exhibits shifts toward more negative potentials as one would expect with increasing sweep rates (Figure S2) due to the slow kinetics of $Ag^+$ reduction at ITO.

Individual diffraction-limited spots (fwhm ≈ 350 nm) were resolved in the scattering images. For data analysis, spot location was carried out through custom MATLAB programs and resulted in several hundreds to thousands being detected per sample.[24] For the sample depicted in Figure 2, 770 spots were detected, resulting in an apparent surface density of $7.55 \times 10^6$ spots·cm$^{-2}$. The average distance between a given spot and its nearest neighbor is ~2.8 $\mu$m. This resulting density can be rationalized by considering the growth of spherical diffusion layers originating from nucleation sites on the electrode surface; the diffusion layer overlapping resulting from the deposition of individual particles would control the effective final particle sizes and density.[25,26] Due to this well documented behavior, and the scanning electron microscopy (SEM) data to be discussed later, the authors are confident that the diffraction limited spots in the final scattering images correspond to either "lone" or a few closely "grouped" particles, though it is likely the observed particles result from several nucleation sites early in the deposition process.

Some example scattering-potential transients for individual spots are given in Figure 3A. The individual scattering transients were fit to obtain distributions of final scattering intensities ($A_{sig}$), as shown in the inset of Figure 3A, and light scattering "turn-on" potentials ($E_{on}$) as shown in Figure 3B. Detailed data fitting procedures are described in the Supporting Information. The distribution of final scattering intensities is obviously correlated with the final shape and size of the particles. $E_{on}$ physically represents the electrode potential at which the scattering of light by the particle becomes detectable, which is dependent on the experimental configuration. For the configuration employed here, the limit of detection in terms of particle diameter is ~46 nm (using a definition of 3 times the detection noise). The distribution in $E_{on}$ values reflects a combination of several factors, including (1) variations in the required overpotential to

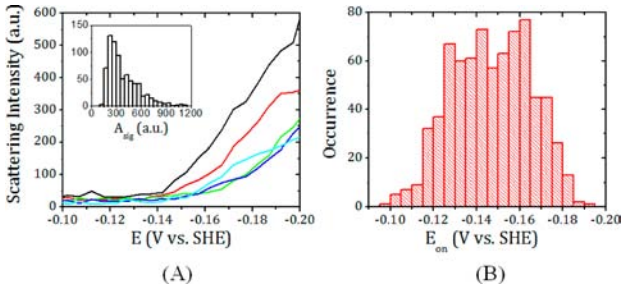


**Figure 3.** Example individual particle scattering transients (A), histograms of the final light scattering intensity ("$A_{sig}$", inset of A), and "turn-on" potential obtained from the data fitting (B).

drive $Ag^+$ reduction at different sites on the ITO surface, (2) the proximity/overpotential of neighboring sites on the surface, and (3) variations in particle geometry and/or orientation with respect to the substrate. The observed $E_{on}$ values span a 60 mV range. Variations in the local overpotential could be due to inherent variations in the defect sites on the ITO surface at which deposition occurs or to local variations in contact area or conductivity of the ITO electrode.[27] The $E_{on}$ and $A_{sig}$ parameter values for individual NPs are found to be weakly correlated, with a more negative turn-on potential corresponding to a smaller final scattering intensity (Figure S7). The weakness of the observed correlation is due to the several competing factors (1−3) mentioned previously. While these results provide some qualitative insight into the heterogeneity in the reduction of $Ag^+$ at ITO, more desirable is quantitative information on fundamental electrochemical parameters (reaction half-potentials, kinetic parameters, etc.) rather than the empirical analysis discussed thus far. This can be done by correlating the observed scattering signal with the actual particle size.

In a simplified sense, the measured scattering intensity can be expressed as

$$I_{obv}(r, \theta_i, \Delta\theta) = \chi \int \sigma_i(k, r, \theta_i, \Delta\theta) I_{lamp}(k) \eta_{CCD}(k) \eta_{coll}(\theta_i)\, dk \quad (1)$$

where $\sigma_i$ is the scattering cross section, $I_{lamp}$ is the lamp intensity profile, and $\eta_{coll}$ and $\eta_{CCD}$ are the collection and detection efficiencies, respectively. $\chi$ is a factor which accounts for the absolute lamp intensity at the sample surface, and is the quantity varied to perform the data fitting discussed later. Calculation of $\sigma_i$ for spherical, homogeneous metal particles can be carried out directly using Mie theory; not knowing explicit values for all of the other quantities prevents one from obtaining a direct relationship between scattering intensity and particle size. To address this issue, correlated SEM measurements were carried out on the deposited particles. The particles corresponding to spots in the scattering image were identified via SEM and sized. Example SEM images can be seen in Figure 4A,B. The image in Figure 4A is overlaid with the scattering image obtained during the deposition process (see Figure S5). Immediately evident is the presence of particles on the ITO surface not visible in the scattering image. These particles are a combination of stray Al particles created during the deposition of the Al index (see the Supporting Information) and deposited Ag particles too small to be detected via scattering. The Al particles (and any other static defect) are ignored in the scattering analysis through a background correction procedure (see the Supporting Information). The SEM analysis made it possible to unambiguously


dx.doi.org/10.1021/ja4075387 | J. Am. Chem. Soc. 2013, 135, 17250−17253

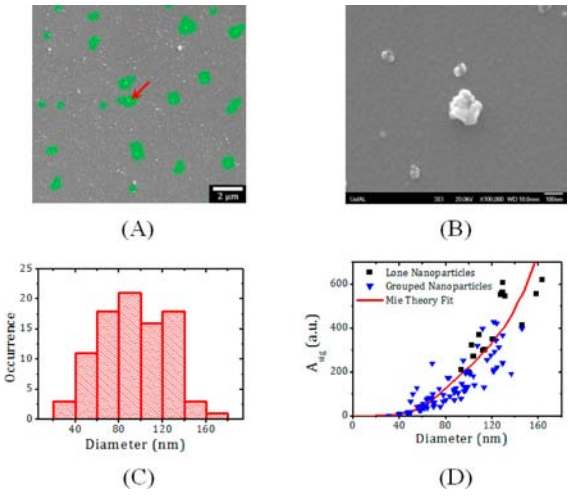


**Figure 4.** Low-magnification SEM image of deposited Ag particles (A), high-magnification SEM image of the indicated particle (B), histogram of particle sizes obtained through SEM analysis (C), and results of single particle scattering-size correlations (D). The transparent green overlay in (A) is generated from the corresponding DFS image (Figure S5).

attribute the spots in the scattering image to scattering from lone or closely grouped particles. Of the ∼40 correlated areas for the sample discussed here, roughly one-third could be unambiguously assigned to individual particles. More careful control over deposition parameters (e.g., employing a dual potential step instead of a sweep) could eliminate this issue by lowering the particle surface density further. The morphology of the deposited particles was found to be roughly spherical in nature. A histogram of obtained particle sizes is given in Figure 4C. The relationship between the scattering intensity and particle size for the lone particles can be observed in Figure 4D (black squares). The proper value of $\chi$ is obtained by a numerical fitting procedure using the scattering intensity values for the lone particles. The result of this fitting procedure is given as the red curve in Figure 4D. For the spots found to correspond to small groups of particles, individual particle intensities can be extracted from the measured intensity according to the theoretical curve profile. The result of this process for the "grouped" spots in the SEM analysis is the blue triangles in Figure 4D. This illustrates that even in cases where a given diffraction-limited spot does not correlate to an individual particle, the Mie theory approximation used in this analysis can still accurately agree with the measured intensity. Detailed information on the calculations discussed here can be found in the Supporting Information.

Once the final scattering intensities have been "calibrated" against the SEM data, it becomes trivial to convert single NP scattering transients into corresponding size transients. This process was carried out blindly for all 770 spots imaged optically. The authors acknowledge that this results in some closely packed groups of particles being treated theoretically as individual particles; the systematic correlation via SEM for hundreds of particles would be ideal but time prohibitive. Once radius potential curves are in hand, it is then possible to estimate the Faradaic current for $Ag^+$ reduction contributing to a given particle's growth (assuming the uniform growth of a homogeneous sphere):

$$i(t) = \left(\frac{4\pi\rho_{Ag}F}{M_{Ag}}\right) r(t)^2 \frac{dr(t)}{dt} \qquad (2)$$

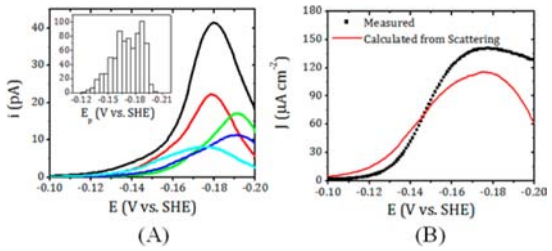


**Figure 5.** Example of reconstructed voltammetric curves for single particles (A), histogram of peak potentials (inset of A), and comparison of measured and calculated bulk current densities obtained through the scattering calculations for all 770 particles (B).

where $\rho_{Ag}$ is the density of Ag, $F$ is Faraday's constant, and $M_{Ag}$ is the atomic weight of Ag. Example single particle voltammograms can be seen in Figure 5A along with the distribution of peak potentials. Using the resulting single particle currents and the observed particle surface density, the bulk Faradaic current density was then estimated from the scattering data and compared to the current density measured by the potentiostat (Figure 5B). The agreement between the calculated and measured current densities is impressive and supports the validity of the single NP scattering analysis. The discrepancy at more cathodic potentials may be due to the presence of undetected Ag particles, differing particle size distributions between the entire working electrode (∼2 $cm^2$) and 100 $\mu$m × 100 $\mu$m imaged area, or to non-Faradaic processes occurring at the working electrode which are effectively ignored in the scattering analysis. Disagreement due to non-Faradaic processes actually highlights an important inherent advantage to this technique: the only processes which contribute to scattering signal are those considerably altering either the morphology of the NP or its surrounding dielectric environment.

It is worth noting that in order to obtain single particle $i$–$E$ curves such as those given in Figure 5, no assumptions about the electrochemical behavior of the system (diffusion behavior, electrode kinetics, etc.) must be made. This is due to the direct correlation between particle size and scattering intensity established through the SEM measurements. However, because the scattering analysis provides no information about an NP's growth until it reaches a detectable size, fitting the data to a theoretical model has value because it can help infer information about the behavior before this point. To this end, a crude model has been developed for fitting the single NP scattering data in terms of the local $Ag^+$ reduction potential and effective electrode area the NP occupies. Details of this model and fitting results are discussed in the Supporting Information.

This technique has also been applied to observe the subsequent oxidation of the electrodeposited Ag particles. The results are given in Figures S8 and S9. Oxidation of the Ag NPs is visible in the cyclic voltammagram at ∼0.2 V vs SHE. This correlates with a drop in total scattering intensity for the ensemble of deposited particles of ∼10%. The relative reduction in scattering intensity for single particles upon oxidation varies from particle to particle, not being visible at all in some cases (e.g., the particle represented by the green curve in Figure S9). Further investigation is needed to establish a firm relationship between size and oxidation potential using the DFS spectroelectrochemical method developed in this work and compare it to reported results from ensemble measurements.[28−31]

Before concluding, several drawbacks to this technique of varying severity should be addressed. First, and perhaps most


dx.doi.org/10.1021/ja4075387 | J. Am. Chem. Soc. 2013, 135, 17250−17253

limiting, is that the individual and closely packed ($d$ < ~350 nm) NPs cannot be distinguished optically. Unfortunately, there is no convenient solution to this issue within the current experimental configuration. An alternate experimental configuration employing a miniaturized light source such as a near-field scanning optical fiber could help improve the spatial resolution, but this would come at the cost of simultaneous multiparticle detection. The surface density of deposited particles could feasibly be reduced to the point where virtually no particles are too close to one another to be resolved optically, but this is certainly not always desirable or even possible. Second, there is a practical lower limit to the detectable particle size (~20 nm in diameter for Ag) for DFS; this problem can be compounded if there is a wide spread in particle sizes. In our measurements, low detector gains and excitation intensities had to be employed to prevent damage to our detector; if the size range was narrower and the surface roughness of ITO was decreased, increased gain/excitation intensity could lower our practical detection limit. Similarly to the previous issue, however, an improvement here may not be possible depending on the system at hand. Third, the transmission geometry employed here requires the use of a transparent electrode, traditionally ITO or FTO (fluorine tin oxide). A backscattering geometry could be employed to perform such experiments at an opaque electrode. Finally, this technique is only feasible for materials exhibiting strong light scattering. However, many such materials are of high academic and industrial importance. The technique we have presented could thus be applied to study their chemistry at the nanometer scale.

To conclude, the tracking of the deposition of individual Ag nanoparticles at ITO has been reported. Through correlation with electron microscopy, the determination of particle size from measured scattering intensities is demonstrated to be possible. This enables the facile reconstruction of voltammetric curves for individual NPs which are inaccessible through traditional electrochemical techniques. The reported technique has the potential to be applied to the study of many other systems of interest in the fields of plasmonics, catalysis, and molecular sensing.

## ■ ASSOCIATED CONTENT

### Supporting Information

Detailed information on sample preparation, experimental procedures, and calculations. This material is available free of charge via the Internet at http://pubs.acs.org.

## ■ AUTHOR INFORMATION


### Corresponding Author

span1@bama.ua.edu


### Notes

The authors declare no competing financial interest.

## ■ ACKNOWLEDGMENTS

This material is based upon work supported by the Department of Energy under Award No. DE-SC0005392. C.M.H. has been partially supported through a Graduate Council Research Fellowship from The University of Alabama and an Alabama EPSCoR GRSP Fellowship. The authors would like to thank Gregory Szulczewski and Edward C. Ellingsworth for performing Al depositions, Daniel A. Clayton for numerous valuable discussions, and Katherine Willets for her suggestions regarding substrate indexing.

## ■ REFERENCES


(1) Xiao, X.; Bard, A. J. *J. Am. Chem. Soc.* **2007**, *129*, 9610−9612.
(2) Han, K. S.; Liu, G.; Zhou, X.; Medina, R. E.; Chen, P. *Nano Lett.* **2012**, *12*, 1253−1259.
(3) Zhou, X.; Xu, W.; Liu, G.; Panda, D.; Chen, P. *J. Am. Chem. Soc.* **2010**, *132*, 138−146.
(4) Xu, W.; Shen, H.; Liu, G.; Chen, P. *Nano Res.* **2009**, *2*, 911−922.
(5) Palacios, R. E.; Fan, F. F.; Bard, A. J.; Barbara, P. F. *J. Am. Chem. Soc.* **2006**, *128*, 9028−9029.
(6) Palacios, R. E.; Fan, F. F.; Grey, J. K.; Suk, J.; Bard, A. J.; Barbara, P. F. *Nat. Mater.* **2007**, *6*, 680−685.
(7) Pan, S.; Wang, G. In *Single-molecule and single-nanoparticle electrochemistry at nanoelectrodes and spectroelectrochemistry*; Pierce, D., Ed.; Trace Analysis with Nanomaterials; Wiley-VCH: Weinheim, 2009.
(8) Shan, X.; Patel, U.; Wang, S.; Iglesias, R.; Tao, N. *Science* **2010**, *327*, 1363−1366.
(9) Wang, S.; Huang, X.; Shan, X.; Foley, K. J.; Tao, N. *Anal. Chem.* **2010**, *82*, 935−941.
(10) Shan, X.; Diez-Perez, I.; Wang, L.; Wiktor, P.; Gu, Y.; Zhang, L.; Wang, W.; Lu, J.; Wang, S.; Gong, Q.; Li, J.; Tao, N. *Nat. Nano* **2012**, *7*, 668−672.
(11) Mock, J. J.; Barbic, M.; Smith, D. R.; Schultz, D. A.; Schultz, S. *J. Chem. Phys.* **2002**, *116*, 6755−6759.
(12) Nehl, C. L.; Grady, N. K.; Goodrich, G. P.; Tam, F.; Halas, N. J.; Hafner, J. H. *Nano Lett.* **2004**, *4*, 2355−2359.
(13) Sherry, L. J.; Chang, S.; Schatz, G. C.; Van Duyne, R. P.; Wiley, B. J.; Xia, Y. *Nano Lett.* **2005**, *5*, 2034−2038.
(14) van Dijk, M. A.; Tchebotareva, A. L.; Orrit, M.; Lippitz, M.; Berciaud, S.; Lasne, D.; Cognet, L.; Lounis, B. *Phys. Chem. Chem. Phys.* **2006**, *8*, 3486−3495.
(15) Novo, C.; Gomez, D.; Perez-Juste, J.; Zhang, Z.; Petrova, H.; Reismann, M.; Mulvaney, P.; Hartland, G. V. *Phys. Chem. Chem. Phys.* **2006**, *8*, 3540−3546.
(16) Sherry, L. J.; Jin, R.; Mirkin, C. A.; Schatz, G. C.; Van Duyne, R. P. *Nano Lett.* **2006**, *6*, 2060−2065.
(17) Hu, M.; Chen, J.; Marquez, M.; Xia, Y.; Hartland, G. V. *J. Phys. Chem. C* **2007**, *111*, 12558−12565.
(18) Munechika, K.; Smith, J. M.; Chen, Y.; Ginger, D. S. *J. Phys. Chem. C* **2007**, *111*, 18906−18911.
(19) Novo, C.; Funston, A. M.; Pastoriza-Santos, I.; Liz-Marzán, L.; Mulvaney, P. *J. Phys. Chem. C* **2008**, *112*, 3−7.
(20) Rodríguez-Fernández, J.; Novo, C.; Myroshnychenko, V.; Funston, A. M.; Sánchez-Iglesias, A.; Pastoriza-Santos, I.; Pérez-Juste, J.; García, d. A.; Liz-Marzán, L. M.; Mulvaney, P. *J. Phys. Chem. C* **2009**, *113*, 18623−18631.
(21) McMahon, J. M.; Wang, Y.; Sherry, L. J.; Van Duyne, R. P.; Marks, L. D.; Gray, S. K.; Schatz, G. C. *J. Phys. Chem. C* **2009**, *113*, 2731−2735.
(22) Knight, M. W.; Wu, Y.; Lassiter, J. B.; Nordlander, P.; Halas, N. J. *Nano Lett.* **2009**, *9*, 2188−2192.
(23) Tcherniak, A.; Ha, J. W.; Dominguez-Medina, S.; Slaughter, L. S.; Link, S. *Nano Lett.* **2010**, *10*, 1398−1404.
(24) Hill, C. M.; Pan, S. *MRS Proc.* **2013**, *1493*, 309−314.
(25) Walter, E. C.; Zach, M. P.; Favier, F.; Murray, B. J.; Inazu, K.; Hemminger, J. C.; Penner, R. M. *ChemPhysChem* **2003**, *4*, 131−138.
(26) El-Deab, M. S.; Sotomura, T.; Ohsaka, T. *J. Electrochem. Soc.* **2005**, *152*, C1−C6.
(27) Liau, Y.; Scherer, N. F.; Rhodes, K. *J. Phys. Chem. B* **2001**, *105*, 3282−3288.
(28) Masitas, R. A.; Zamborini, F. P. *J. Am. Chem. Soc.* **2012**, *134*, 5014−5017.
(29) Ivanova, O. S.; Zamborini, F. P. *Anal. Chem.* **2010**, *82*, 5844−5850.
(30) Ward Jones, S. E.; Campbell, F. W.; Baron, R.; Xiao, L.; Compton, R. G. *J. Phys. Chem. C* **2008**, *112*, 17820−17827.
(31) Ivanova, O. S.; Zamborini, F. P. *J. Am. Chem. Soc.* **2010**, *132*, 70−72.